Characterization of plastic deformation induced by machining in a Ni-based superalloy

Ding, Rengen; Knaggs, Craig; Li, Hangyue; Li, Yue Gang; Bowen, Paul

DOI:
10.1016/j.msea.2020.139104

Document Version
Peer reviewed version

Citation for published version (Harvard):
Ding, R, Knaggs, C, Li, H, Li, YG & Bowen, P 2020, 'Characterization of plastic deformation induced by machining in a Ni-based superalloy', *Materials Science and Engineering A*, vol. 778, 139104, pp. 1-13. https://doi.org/10.1016/j.msea.2020.139104

Journal Pre-proof

Characterization of plastic deformation induced by machining in a Ni-based superalloy

Rengen Ding, Craig Knaggs, Hangyue Li, Yue Gang Li, Paul Bowen

PII: S0921-5093(20)30192-1

DOI: https://doi.org/10.1016/j.msea.2020.139104

Reference: MSA 139104

To appear in: *Materials Science & Engineering A*

Received Date: 15 November 2019

Revised Date: 11 February 2020

Accepted Date: 12 February 2020

Please cite this article as: R. Ding, C. Knaggs, H. Li, Y.G. Li, P. Bowen, Characterization of plastic deformation induced by machining in a Ni-based superalloy, *Materials Science & Engineering A* (2020), doi: https://doi.org/10.1016/j.msea.2020.139104.

Credit Author Statement

R.Ding: Conceptualization, Methodology, Investigation, Formal analysis, Data curation, Visualization, Writing. **C. Knaggs:** Investigation, Data curation. **H.Y. Li:** Conceptualization, Validation, Review. **Y.G.Li**: Conceptualization, Resources, Review. **P. Bowen:** Resources, Review.

Characterization of plastic deformation induced by machining in a Ni-based superalloy

Rengen Ding[a], Craig Knaggs[a], Hangyue Li[a], Yue Gang Li[b], Paul Bowen[a]

a*: School of Metallurgy and Materials, University of Birmingham, Birmingham, B15 2TT, UK*
b:Rolls-Royce plc., PO box 31, Derby, DE24 8BJ, UK

Abstract

The surface integrity characteristics of Udimet 720Li subjected to slight damage and damage machining conditions have been studied using a complementary range of techniques such as FIB-SEM, EBSD, TKD, TEM-EDS and nano-indentation. The results indicate the existence of nano-sized grains and no observable tertiary γ' in regions of severe plastic deformation in the machined surface. The correlation between the machining condition and the resulting plastic deformation is established. Grain refinement of this alloy via machining was achieved by dislocation slip. The nanohardness of the surface of damage machined sample is 40% higher than that of bulk material, which is attributed to the formation of nano-sized grains and high density of dislocations in the superficial layer.

Keywords: Ni-based superalloy; Machining; FIB; TEM

1. Introduction

Ni-based superalloys are used extensively in aerospace due to their ability to retain high strength at elevated temperature over the operating life, in addition to strong chemical and thermal stability [1-3]. Ezugwu [1] has classified this class of materials as ‘difficult-to-machine’ on the base of their physical properties and machining characteristics. Many factors contribute to this involving low thermal conductivity, resulting in high cutting temperatures at the rake face and associated accelerated tool flank wear. Other factors involve rapid work hardening of the matrix during machining, the presence of various hard abrasive precipitates (i.e. carbides) that speed up flank wear, and the tendency for built-up-edge formation resulting in poor surface roughness [4]. Thus, machining of Ni-based superalloys is very challenging.

Complex aeroengine components demand that careful processing routes are used to ensure robust manufacture from forging to the finishing cutting operation [5]. In particular, the quality of the surface of the rotating parts must be considered carefully because they could become fatigue initiators [6]. Factors such as surface roughness, residual stress and workpiece surface integrity (e.g. metallurgical change on/beneath the machined surface) can

potentially reduce fatigue life [7, 8]. Thus, many studies of these three topics have been performed [4, 5, 7, 9-15]. Since it has been well documented that compressive residual stress is beneficial to fatigue properties, some studies evaluating residual stress or/and stress relaxation under elevated temperature exposure and under isothermal fatigue [4, 5, 9-12] have been performed. Novovic [7] has reviewed the published data on the effect of surface topography on fatigue life and concludes that, in most cases, lower roughness leads to longer fatigue life but that for roughness values in the range 2.5-5 μm Ra fatigue life is primarily dependent on workpiece residual stress and surface microstructure, rather than on roughness. During machining involving excessive cutting speeds or dry cutting conditions large strains may develop at or underneath the surface of the workpiece and temperatures as high as 600-1300°C can be reached for Inconel 718 [13], which could lead to the formation of a distinct surface layer having very different properties from the bulk material [14, 15] and the formation of a thin oxide on the surface. This distinct near surface layer usually has a fine microstructure (e.g. nano-grains), which can improve the resistance to fatigue crack initiation [16, 17]. Surface severe plastic deformation (S^2PD) has been considered as an effective approach for producing engineering parts with a surface nanocrystalline layer but a coarse-grained interior. One popular S^2PD technique is shot-peening. A study of a nickel-base alloy showed a 50% improvement in fatigue life after S^2PD processing [18]. A 65-84 % increase in the 0.2% offset yield strength of a nickel-base alloy has also been observed [19]. In order to understand the improvement of the mechanical properties of the materials, many studies [20-23] have focused on the metallurgical features of the surface/subsurface layer. The improvement in the mechanical properties is ascribed to the formation of refined grains at the surface region accompanied by high densities of dislocations, faults and twins as well as a macroscopic residual stress [24].

The methods for investigating severely deformed layers include optical microscopy, scanning electron microscopy (SEM) [5, 25], X-ray diffraction [9, 24], electron backscattered diffraction (EBSD) [11, 12, 20] and hardness testing. Transmission electron microscopy (TEM) has been proved an invaluable method for characterising severely deformed microstructures [20-23, 26, 27]. Two methods for preparing TEM specimens are conventionally used: 1) a cross-section through the surface plus ion-milling: the method permits the investigation on the microstructural evolution from the surface to the interior of the sample but a continuous and complete thin region starting at the surface and ending in the bulk may not be achieved. In other words, this method may not give us an overview of the surface and subsurface. 2) plan-view plus twin-jet polishing: the surface is protected by loctite during perforation [20, 21]. This allows a study of the surface but it is difficult to

characterise the surface contamination (e.g a ~ 30 nm oxide such as observed in this work) produced by S^2PD processing. Recently, focused ion beam microscopy (FIB) has been used extensively to make TEM specimens with the surface protected. As a site-specific method, FIB can also extract TEM foils from machining defects etc.. For example, Saoubi et al. [22, 23] used FIB to prepare TEM specimens in order to examine the deformed microstructure of machined Ni-base alloys, but there was no information given on microstructure or the behaviour of γ' at the surface. Very recently, Liao et al. [28] used EBSD plus FIB to investigate the formation mechanism of white (surface) layer of a next generation Ni-base superalloy (S135H) produced by severe plastic deformation and found that the surface layer is softer than the subsurface, which is attributed to the dissolution of γ' at the surface. This finding is not consistent with some of previous studies. Chen et al. [29] employed TEM and transmission Kikuchi diffraction (TKD) to study the formation mechanism of the white layer produced by broaching in IN718 and observed Al-rich and Nb-rich cluster at the surface layer. In a word, previous investigations have proved that the surface-hardened layer development and the underlying formation mechanism are strongly dependent on the materials and the machining conditions.

Udimet 720Li is a relatively new polycrystalline nickel-base superalloy, conceived in the late 1990s [30]. This alloy has received widespread use in aeroengine turbine discs at temperatures as high as 600°C to 700°C [31]. Although careful processing routes are usually used to machine the discs from the forged alloy right through to the finishing cutting operation, some incidents (e.g. the tool breaking) during machining may bring about surface anomalies (e.g. roughness) of the discs outside the specification. Such anomalous surface may degrade potential properties (e.g. life) of the discs. It is thus of key importance to study the surface-hardened layer development and its formation mechanism of 720Li samples machined by different damage conditions.

In this paper, hardness tests, SEM and EBSD were used to characterize the work-hardened layer. The strength of severe plastic deformation layer was evaluated using microcompression. Cross-section TEM specimens from the machined surfaces were prepared by FIB, which give us the opportunity to examine in detail the surface microstructure, including γ' and surface oxidation.

2. Experimental Procedure

2.1 Material and Specimens

The chemical composition of the Ni-based superalloy Udimet 720Li is listed in Table 1. To investigate the effect of surface condition on the fatigue properties of the alloy, test-pieces

were machined with two sets of machining: 1) speed 254 rpm, feed rate 24 mm/min, 2) speed 5000 rpm, feed rate 4000 mm/min. These resulted in surface roughness Ra values of 0.29 microns for '1' and 1.82 microns for '2', respectively. These two sets of test-pieces are referred to as 'slightly damaged' and 'damaged' (Fig. 1). A worn tool was used for damage-machined samples to encourage sub-surface plastic deformation. Test-pieces were extracted from a disc scrapped at finish-machining stage. It should be mentioned here that those machining conditions are purely designed to generate damage. Even for 'slight damaged' samples, their machining parameters are not for machining disc. The microstructure consists of a matrix of γ with a mean grain size of 12 μm and a trimodal distribution of γ′ precipitates (primary, secondary and tertiary) (Fig. 2 and Table 2). The microstructure also contains small TiC precipitates (not shown here).

2.2 Mechanical properties

Hardness maps were obtained using a Durascan hardness tester on samples cross sections. The load used during the measurements was 0.1kg. 400 indents were made in a rectangular area 0.5 mm deep and 2 mm wide. The corresponding hardness values were processed using a MATLAB script to produce the depth of the affected material. In addition, a through-depth hardness profile was determined using a nanotest system (Micro Materials Ltd, Wrexham, UK) XP fitted with a Berkovich tip, again on a cross section. The maximum load of 40 mN was applied for a 30 s period. The hardness was calculated using the equation.

$$H = \frac{P_{max}}{A_c}$$

where A_c is the projected contact area at the maximum load P_{max}.

To study mechanical properties of the severe deformed layer, micro-compression was performed in-situ using a Hysitron PI85 picoindenter mounted inside a Tescan Mira-3 SEM using a flat puncher with 20μm diameter under displacement-controlled mode with the displacement rate of 1 nm/s. The square micro-pillars of ~3μm were prepared near the machined surface using an FEI Quanta 3D FIB system.

2.3 Scanning Electron Microscopy – EBSD

Specimens were cross-sectioned from those two sets of test-pieces. The specimens were mounted in a conductive Bakelite to produce sharp edges and aid EBSD sample preparation. The specimens were mechanically ground, and polished using colloidal silica for 30 min to obtain a surface suitable for EBSD analysis. EBSD data were acquired with HKL Channel 5 software using a scan area of 265 μm × 260 μm and a step size of 0.5 μm, with an accelerating voltage of 20 kV, a sample working distance of 20 mm and sample tilt of 70°.

The HKL Tango Maps package with low-noise filtering was applied and the wild spikes removed. Local misorientation maps use the average misorientation between each measurement and its 8 neighbours, excluding higher angle boundaries (5 degrees).

2.4 Transmission Electron Microscopy and Transmission Kikuchi Diffraction (TKD)

To investigate the microstructure of the severely plastically deformed surface/subsurface, the FIB lift-out method in an FEI Quanta 3D FIB system was used to prepare TEM samples. For the 'damaged' sample, in addition to machining marks, the defects (referred to as a 'ramp' here) were found on the surface (Fig. 3b). Therefore, two samples were lifted out from the damaged sample. One is sectioned across the ramp arrowed in Fig. 3b, the other is from a 'normal' region shown in Fig. 3b. The examinations were carried out in an FEI Tecnai F20 field emission gun scanning transmission electron microscope (FEG-STEM) equipped with an Oxford Instruments Silicon Drift Detector (SDD) for energy – dispersive X-ray spectrometry (EDS) at 200 kV. Due to severe plastic deformation it is very difficult to show the distribution of small γ' precipitates (e.g. secondary and tertiary) in imaging mode. EDS was therefore used to explore the distribution of the small γ' precipitates and surface oxides.

Although most studies of nanostructure characterisation have utilised TEM, grain size analysis using bright or dark field images in TEM is challenging. Furthermore, although automated diffraction techniques do exist for the TEM, they generally suffer from slow data collection and only small regions can be analysed [32]. Moreover, the novel 'TKD' technique has been demonstrated to be powerful at revealing nano-sized substructure in highly deformed materials [33] and machining induced surface layer [28, 29]. The sample for TKD is electron-transparent and mounted horizontally or back-tilted away from the EBSD detector. The Kikuchi patterns are generated mainly from the bottom surface of the sample with a small source volume, which improves the spatial resolution from ~ 20nm in conventional EBSD down to ~ 5nm. Additionally, conventional EBSD analysis of highly deformed regions is always problematic due to lattice distortion and the high dislocation density, which leads to blurring and even absence of the Kikuchi patterns, thus leading to poor indexing accuracy. This situation is alleviated when TKD is applied, due to its smaller interaction volume, which enables the indexing of regions with heavy plastic deformation. Thus, in this study, the Fibbed TEM foil was used to perform TKD with a 10 nm step size so as to characterise the nanostructure and crystallographic texture of the deformed layer induced by machining.

3. Results and analysis

3.1 SEM and EBSD analysis

Figure 4 shows SEM images of the slightly damaged and damaged specimens. In the slightly damaged specimen, primary γ′ precipitates very close to the surface were observed to be severely deformed (Fig. 4a). Closer examination also shows deformed secondary and tertiary γ′ precipitates (Fig. 4b). The depth of work-hardening caused by machining can be estimated via shear bands and/or deformed γ′ precipitates. A shear band (arrowed in inset to Fig. 4a) was found at 33 μm from the surface. In other words, the depth of work-hardening is at least 33 μm in the slightly damaged specimen. It is interesting that there is a layer with a thickness of ~ 400 nm, where there are 'no observable particles' (e.g. γ′ precipitates) (inset to Fig. 4b). Compared to the slightly damaged specimen (Fig. 4a), deformed primary γ′ precipitates are observed over a deeper region from the surface of the damaged specimen (Fig. 4c). Sheared secondary and tertiary γ′ precipitates (dark arrows) are clearly shown in the inset to Fig. 4c, which was taken from the position indicated by a white arrow in Fig. 4c, 140 μm away from the surface. The shear strain estimated from the sheared secondary γ′ precipitates (arrowed in inset to Fig. 4c) is ~14%. Therefore, the depth of work-hardening in the damaged specimen is larger than 140 μm. Careful observation found that there is a wavelike layer with a width of 800 – 1200 nm (inset to Fig. 4d) (where the microstructural details were not explored), which is wider than that observed in the slightly damaged specimen (~400 nm). From SEM observation, we know that primary γ′ precipitates at the surface were not dissolved during machining while tertiary γ′ precipitates may be dissolved. This is consistent with the fact that the solvus temperature of primary γ′ is much higher than that of tertiary γ′ precipitates. As expected, worn tool machining gives rise to a deeper severely plastically deformed region. It should be mentioned here that the machining defects such as those arrowed in Fig. 3b were not found in the cross-section SEM specimen although it is not very difficult to find such defects on the machined surface of the damaged specimen.

EBSD is able to provide comprehensive information about the local grain structure at the machined surface. EBSD data were used to measure the thickness of the deformed layer (work hardening) in terms of the deviation from the grain average orientation. Figs. 5a and 5b show EBSD inverse pole figure maps of the slightly damaged and damaged specimens. There is no clear evidence of recrystallization in the near surface of the slightly damaged specimen (Fig. 5a). For the damaged specimen, however, there is a clear recrystallized region beginning at the machining surface and ending between 50-80 μm away from the surface (Fig. 5b). Away from the recrystallized region, a region with elongated grains was observed (Fig. 5b). Fig. 5b also shows that the amount of non-indexed points is greater close to the

surface, which is due to the difficulty of indexing patterns in regions of severe deformation. To visualise the extent of plastic deformation near the machined surface, local misorientation maps are given in Figs. 5c and 5d, which also show the heterogeneity within the deformed region. Such heterogeneity could be related to local grain orientation. As expected, regions of increasing strain are located near the machined surface (green-yellow-red colour) and regions of low strain near the bulk (blue colour). The extent of plastic deformation below the subsurface can thus be estimated: ~ 40 μm and ~ 200 μm for the slightly damaged and damaged specimens, respectively. Both are similar to the SEM results (33 μm for slightly damaged vs. 140 μm for damaged sample). 40 μm thick plastic deformation below the surface of the slightly damaged specimen is compared with 60 μm plastic deformation produced by abrasive drilling in alloy Udimet 720Li [22].

Although EBSD can be used to evaluated crystal rotation and related dislocation density (i.e. geometrically necessary dislocations (GNDs)), it cannot help to identify the deformation mechanism or measure the true dislocation density, particularly if the deformation is concentrated into shear bands. In this case, the orientation of the crystal on each side of the dislocation shear bands is the same; this deformation mechanism is clearly visible in the SEM (inset to Fig. 4c). Therefore, EBSD cannot provide a whole picture regarding the deformation mechanisms related to machining, including the effects of the γ′ precipitates. Also, EBSD spatial resolution limits the analysis of nanocrystalline (nc) grains in bulk specimens. Further complementary techniques (e.g. TEM plus EDS) are needed and are given in the TEM section below.

3.2 Hardness and strength

Microhardness measurements were tested in cross-section from the machined surface of each of the specimens to evaluate work hardening. Figure 6 shows hardness maps for the slightly damaged and damaged specimens beginning from the machined surface and ending 500 μm into the specimen. The depth of work-hardening is estimated to be ~ 200 μm for the damaged specimen (Fig. 6b), which is in a good agreement with the value measured via EBSD. This value is similar to others published for shot-peened 720Li [1, 2]. Child et al. observed that the depth of the hardness affected zone is in the range of 100~250 μm for different shot-peened 720Li specimen [2]. The hardness map (Fig. 6a) does not reveal any work-hardening in the slightly damaged specimen, which is attributed to: 1) narrow work-hardening zone of 40 μm (as measured by EBSD), and 2) widely spaced indents (50 μm). Thus, a nanoindenter was used to measure the hardness profiles (as shown in Fig. 6c), which show that the depth of

work-hardening is ~ 20 μm for the slightly damaged specimen, but ~ 220 μm for the damaged specimen (this value is consistent with the results from the microhardness tester). It should be noted that the hardness close to the surface for the slightly damaged specimen is much lower than that for the damaged specimen, which is probably associated with their deformed microstructures. This issue will be discussed in section 3.3.

The strength of the severe plastic deformation layer of the damage sample was evaluated using microcompression. Their true stress-strain curves are illustrated in Fig. 7, showing that the yield strength of the severe deformation layer is ~2000 MPa, which is near twice of the bulk. This observation is similar to the results of the shot-peened RR1000, which shows that the strength of the shot-peened surface is close to twice of the bulk [20]. Here it should be mentioned that micropillar was not machined from the bulk because the size of pillar is much smaller than that of grain size (i.e. 3 μm for pillar vs. 12 μm for the bulk). In other words, if micropillar were machined from the bulk, the micropillar may be from a grain, thus it's strength depends on the orientation of grain. However, the micropillar machined from the severe deformation layer contains many grains because there are nano-sized grains in the severe deformation layer (see below).

3.3 Transmission Electron Microscopy

From the SEM observations, we cannot understand the microstructure of the surface layers (~ 400 nm (Fig. 4b) for the slightly damaged specimen and ~ 1000 nm (Fig. 4d) for the damaged specimen). TEM specimens sectioned from the surfaces by FIB permit us to understand the microstructural details of the machined surfaces. A montage of BF-STEM images from the slightly damaged specimen is shown in Fig. 8a, which illustrates there are two distinguishable regions: the region beginning at the surface and ending between 0.6-2 μm away from the surface has a very fine microstructure; in the region below, there is a deformed layer where the grains were elongated and bent, along with slip bands and a very high dislocation density. The microstructure below this deformed layer is the typical fine-grained γ matrix with γ' precipitates. A TEM image taken from the top region is illustrated in Fig. 8b, which shows the formation of nanocrystalline (nc) grains at the machined surface. The average grain size, estimated from TEM images of the nc layer, is 21±5 nm, which is in good agreement with observations on shot-peened C-2000 superalloy [24]. In low-speed milled IN100 Ni-based superalloy, it was observed that the surface nc layer varied in thickness from 0.5-1 μm and that the grain size was in the range 15 to 70 nm [34]. These microstructural features also suggest that dynamic recovery and recrystallization occurred during machining. The selected area diffraction (SAD) pattern from Fig. 8b shows polycrystallinity. The presence of some

arcs in the SAD pattern indicates that the orientation of the nc grains is not completely random, which might be related to the fact that many of them may originate from one large parent grain. EDS was used to reveal what happened to γ′ precipitates at the surface. EDS maps show that there is a region, where γ′ is not observable ~170 nm in depth from the surface (Fig. 8), which suggests that the surface was subjected to a high temperature (higher than the tertiary γ′ solvus temperature) during machining. Heavily deformed (elongated) γ′ precipitates were observed below the no observable γ′ region (Fig. 9) but not revealed by TEM images (Fig. 8 and Fig. 9a). EDS maps also show no evidence of the surface oxidation (Fig. 9).

Figure 10 illustrates a montage of BF-STEM images taken from the 'normal' region of the damaged specimen, showing that there is fine structure close to the surface and that band-like structures are visible with increasing distance away from the surface. The fine structure consists of nc grains (inset to Fig. 10a and Fig. 10b), which is also confirmed by SAD (Fig. 10c). Although the presence of some arcs in the SAD patterns is visible (Fig. 10c), the arcs are not as large as those in the slightly damaged specimen. This means that the nc grains are more random as compared to the slightly damaged specimen, which might be related to: recrystallization being nearly complete and to grain growth (which is also confirmed by the larger average grain size observed in the damaged specimen (41±19 nm) vs. 21±5 nm in the slightly damaged specimen). Moving away from the surface, the microstructure displays band-like feature. The broken rings and large arcs in SAD (Fig. 10e) recorded from the regions with bands, and the preferential intensity distribution around particular orientations indicates an increase in the grain size and the presence of preferred orientation (i.e. shear texture) developed under deformation. The nanostructure and crystallographic texture of the deformed layer are also revealed by TKD, as shown in Fig. 11. In the superficial layer, there can be divided into three regions: recrystallisation, dynamic recovery and grain deformation (Fig. 11a). The surface microstructure shows equiaxed grains with a weak texture (~ 4 times random) (Figs. 11 a and b), which is consistent with the presence of small arcs in the SAD patterns (Fig. 10c). The region in the middle of Fig. 10a, shows elongated grains where some subgrains are visible (Fig. 11c). These elongated grains show a strong texture (~28 times random) (Fig. 11d), which was also confirmed by the presence of large arcs in the SAD patterns (Fig. 10e). The formation of some fine grains (arrowed in Fig. 11c) probably occurs along prior austenite grain boundaries. This study has therefore also demonstrated that TKD is capable of revealing clearly the nanostructure of the deformed layer induced by machining [28, 29].

Fig. 12 shows EDS maps from the region close to the surface, showing a ~ 600 nm wide region where the tertiary γ′ precipitates have disappeared but elongated secondary γ′ precipitates are still present due to the short temperature dwell time of the cutting edge engagement with the respective zone of the workpiece. This agrees with the fact that the solvus temperature of the tertiary γ′ phase is lowest. This region is thicker than that in the slightly damaged specimen (~ 600 nm vs. ~ 170 nm for the slightly damaged specimen), indicating that the surface of the damaged sample reached a higher temperature for a longer time compared with the slightly damaged sample. The oxygen map does not show the existence of surface oxide (Fig. 12).

On the surface of the damaged specimen, defects (such as those denoted as 'ramp') were observed (Fig. 3) which might become stress-concentration sites during fatigue. Microstructural analysis of the ramps is beneficial to understanding their formation mechanism and potential influence on fatigue properties. A montage of BF-STEM images taken from a ramp (arrowed in Fig. 3) is presented in Fig. 13, which clearly shows nc grains in the ramp and coarser grains closer to the surface. A TEM image recorded from the surface of the ramp (Fig. 13c), shows that the average grain size is ~180±56 nm (Table 3), which is significantly larger than that in the 'normal' region of the damaged specimen (41±19 nm). This might mean that recrystallization is nearly complete and that grains have started to grow in the surface of the ramp. The low density of dislocations (Fig. 13c) is the evidence of the recrystallization being nearly complete. These help the grains to lose the orientation of parent grain. In other words, these grains might lose their texture, which is confirmed by there being no clear arcs in the SAD pattern (Fig. 13d). Moving away from the ramp, the boundaries of the nc grains become unclear. An example is shown in Fig. 13e, which was taken from the region marked '1' in Fig. 13a. Its SAD shows ring patterns (which indicate more nc grains) and longer arcs of the patterns (which mean a stronger texture as compared with the surface of the ramp). In the region 14 μm away (or far away) from the surface of the ramp, band-like features become clear (Fig. 13g), showing a stronger texture which is demonstrated by longer arcs in its SAD pattern (Fig. 13h). Compared to the middle region (Figs 13e and f), fewer number of the spots and longer arcs in the patterns were observed in the region 14 μm away from the surface of the ramp, which means less grains and a higher texture in that region. This also indicates that only some grains with a specific orientation deformed.

Figure 14 shows an electron image and the corresponding EDS maps through the surface of the ramp. Clear grains and grain boundaries are visible in the electron image of Fig. 14. EDS maps show there is no evidence of γ′ while Cr and Co are rich in the grain interiors. An interesting observation is Ti enrichment at the grain boundaries (Fig. 14). Partitioning of Cr,

Co and Ti indicates that the immediate subsurface of the ramp has stayed for a certain time at a high temperature. From the electron images of the surfaces (Fig. 13) and the corresponding EDS maps (Fig. 14), there is a region where the tertiary γ′ is not observable and in which nc is also visible. The surface layer has no tertiary γ′ and coarser nc grains, which suggests that the surface is soft compared to the subsurface.

4. Discussion

An investigation with TEM combined with TKD gave us the most direct and accurate picture of the deformed microstructure and helped understand the mechanical behaviour (e.g. hardness and strength) of the machined layers. It was found that recrystallisation took place at the surfaces for both the slightly damaged and damaged samples. A clear difference in hardness between the two samples was observed. The detailed TEM work gives us a chance to explore the hardness difference and the mechanism of grain refinement. The section 4 will focus on those aspects.

4.1 Recrystallisation and estimation of cutting temperature

Kim et al. [9] investigated residual stress in and work hardening of shot-peened 720Li after thermal exposure at different temperatures (i.e. 350°C, 550°C, 650°C, 700°C, and 725°C). Exposure at 350°C relieved the stress only to a small extent while significant recovery was observed at 650°C. To estimate the recrystallisation temperature of the machined surface structures, the chips were heated in a differential scanning calorimeter at a rate of 10°C /min. The DSC scan in Fig. 15 shows a maximum rate of heat evolution occurring at ~ 490°C. This temperature is much higher than the dislocation annealing (recovery) temperature of severely plastically deformed Ni samples, ~ 300°C (depends on shear strains and impurity) [35]. Impurities raise the recrystallization temperature and was ascribed to a decreased dislocation mobility in lower purity Ni due to the dislocation interactions with impurity atoms. The presence of the γ′ precipitates also impedes recovery. It is, thus, not surprising that 720Li alloy has a much higher recovery temperature than severely plastically deformed Ni.

Although the cutting temperature was not measured in this study, previous investigations [22, 35] reported values of 600-900°C (related to cutting speed) for FGH95 Ni-based superalloy [36] and ~ 750°C during drilling of 720Li [22]. We can estimate the cutting temperature in terms of the behaviour of tertiary γ′ in the machined layer. For example, EDS and EBSD results have demonstrated that there is a region where original tertiary γ′ disappears and recrystallisation occurs for both the slightly damaged and damaged samples (Figs. 9, 11 and

12), which suggests that the temperature of the sample surfaces produced by the machining is over the solvus temperature of tertiary γ′ and recrystallisation temperature. Although no data on the tertiary γ′ solvus temperature is available in the open literature, a study of the thermal stability of tertiary γ′ of aged 720Li at 650°C and 700°C has shown that the tertiary γ′ dissolves at 700°C but not at 650°C [37]. This means that the tertiary γ′ solvus temperature is not higher than 700°C but higher than 650°C. Since duration of a heating cycle during machining is very short, the finding of the region where original tertiary γ′ dissolved means that the cutting temperature is much higher than the tertiary γ′ solvus temperature. Thus, it is not unreasonable that the cutting temperature for the slightly damaged sample must be over 650°C although the machining induced a high density of dislocations and a large stored energy, which could reduce the solvus temperature of tertiary γ′. Additionally, it is well known that γ′ precipitates are believed to impinge grain growth. The strength of the pinning effect depends on the volume fraction (F_v) and particle size (r) of the γ′, and it is generally accepted that if $F_v/r > 0.15\ \mu m^{-1}$, recrystallization will be inhibited [38]. This indicates that the recrystallisation region could be larger than the tertiary γ′ dissolved region, which is supported by Fig. 9.

4.2 Hardness

Microhardness testing did not reveal any work-hardening of the slightly damaged sample, which could be related to widely spaced indents (~ 50 μm) and/or a narrow work-hardening zone (Fig. 8a). However, nanoindents showed that the hardness revealed by the first indent (~ 4 μm away from the surface) is slightly higher than the baseline value, which is supported by the microstructure at the centre of Fig. 8a (~ 4 μm away from the surface) exhibiting a high density of dislocations and slip bands. In the damaged sample, moreover, the hardness values from both the microindents (Fig. 6b) and nanoindents (Fig. 6c) reach 140% of the baseline value and are strongly localized within 20 μm of the surface. This finding is associated with high strain, e.g. heavy deformed γ′ observed as in the SEM image (Fig. 4c). High strain also led to poor indexing in EBSD (Fig. 5). The increase in hardness was reflected by the microstructure. For example, in Fig. 10a, the microstructure within 10 μm of the surface consists of nc grains and a high density of dislocations and slip bands. Here, it should be noted that, although in the slightly damaged sample a very fine microstructure (i.e. nc grains combined with a high density of dislocations) was also observed in the region beginning at the surface and ending between 300-800 nm away (Fig. 8), the nanoindenter did not measure

this region. The hardness values of the first indent (~ 4 μm away from the surface) are from large grains with a high density of dislocations and slip bands for the slightly damaged sample (as seen in Fig. 8a) and nc grains with a high density of dislocations for the damaged sample (Fig. 10a). Thus, the observed hardness value of the first indent for the damaged sample is much higher than that for the slightly damaged sample (Fig. 6). Messé et al. [20] observed that the hardness of the surface of shot-peened RR1000 reaches 180% of the baseline value but there was no evidence of recrystallization. The surface hardness of the drilled 720Li is 120% of the baseline value but there was recrystallization [22]. Child et al. [12] found that shot-peening makes the surface hardness increase by 30% for 720Li. These discrepancies are attributed to different deformation microstructures.

4.3 Formation of the nanocrystalline surface

Many investigations of the formation of a nanocrystalline surface during severe surface plastic deformation processes have been performed in a variety of metals and alloys, such as pure Fe, pure Co and pure Cu, stainless steels, carbon steels, Inconel 600Ni, C-2000Ni and Al-based alloys. These works have revealed that the grain refinement mechanisms depend on not only the crystal structure of the materials but also the extrinsic deformation conditions. Plastic deformation of metals can be commonly accommodated by twinning and slip. Plastic straining produces a high density of dislocations in the original grains. Those dislocations re-arrange into different configurations relying on the crystal structure of the metals, including dense dislocation walls on specific slip planes, dislocation tangles, and dislocation cells [39]. Dislocation interactions result in formation of subgrain boundaries with small misorientations. With increasing strain, further development of the sub-boundaries leads to high-angle grain boundaries that subdivide the original grains. These mechanisms commonly describe the grain refinement of the metals with high stacking fault energies (SFE), such as Ni (128 mJ/m^2) and Al (166 mJ/m^2) [40]. Twinning is favourable for metals with low SFE, especially at high strain rates and/or low deformation temperatures. Thus, the grain refinement for those metals is mainly achieved via formation of deformation microtwins and subsequent twin-twin intersections [40] or interactions of microtwins with dislocations inside the twin and matrix [41]. Twinning has been demonstrated in a surface mechanical attrition treated single phase Inconel 600 [41] (which has low-medium SFE (28 mJ/m^2) [42]) and in a severely surface plastically deformed C-2000 alloy with an extremely low SFE (1.22 mJ/m^2) [21]. It should be mentioned that the methods producing serve plastic deformation in both these alloys did not cause a high temperature at the surfaces of the alloys.

The TKD and TEM observations can be used to assert the mechanism of grain refinement of the machined layer. In 720Li alloy no twinning was observed in the deformed region. Clearly, the grain refinement induced via machining was achieved by dislocation slip, as revealed in Fig. 8a. In the region (e.g. the centre bottom of Fig. 8a) with relatively low strain, multiple slip systems are activated and a high density of dislocations is found while the original grain is not obviously deformed. With increasing strain and strain rate induced by machining, a higher density of dislocations is produced, which develops into dislocation tangles and walls, leading to storage of the system energy in form of crystalline defects (Fig. 8a), and which results in the formation of elongated grain via rotational mechanism. Then, the elongated grains can be subdivided into dislocations cells via those dislocation tangles and dislocation walls (Fig. 8a). At the same time, the massive dislocations could bow around γ' precipitates or cut them with coupled dislocations, leading to heavy plastic deformation of those γ' particles (Figs. 4 and 9). With the further increase of strain and strain rate with closing to the machining surface, a density of dislocations is further improved. In order to reduce the stored energy, the dislocation cells will absorb the dislocations and evolve into subgrains with low misorientation (Fig. 11c), thus still keeping a strong texture (Figs. 10e and 11d). In this stage, dynamic recovery dominates the grain development. In superficial layer, cutting temperature reaches the highest value, which causes tertiary γ' particles fully dissolved (Figs. 9, 12, and 14). At the meantime, higher cutting temperature accelerates atomic diffusion of γ'/γ constituent elements, thus promoting that the subgrains absorb the dislocations and the grain boundary angles increases. This process brings about the annihilation and rearrangement of dislocations and the growth of recrystallised grains, thus leading to the formation of more grains with low density of dislocations and high misorientation. Eventually, the texture of the superficial layer becomes more random, as evident in Figs. 10c, 11b, and 13d. It is thus considered that in superficial layer dynamic recrystallisation dominates grain structure evolution. To better describe the microstructural evolution of alloy 720Li during machining, a schematic diagram summarising the major aspects of the deformation microstructures formed in different regions (subsurface and surface) during machining is given in figure 15.

Conclusions

Surface integrity characteristics of machined Udimet 720Li with slight damage and damage conditions have been investigated using FIB-SEM, EBSD, TEM-EDS, nano-indentation and microcompression. The following conclusions can be drawn.

1. Nanoindentation, SEM, EBSD and TEM are complementary techniques to characterize the work-hardened layer induced by machining.
2. The slight damage machining brings about the formation of a 0.6~2 μm deep layer with nano-sized grains from the machined surface. Compared to the slight damage machining, a deeper layer with larger nano-sized grains was observed in the damaged sample, thus showing a clear profile of hardness variation revealed by nanoindentation.
3. Regions with no observable tertiary γ′ in the machined surface were found in all the samples, but the deeper region was observed in the damage sample.
4. In the ramps of the damaged sample, in addition to coarse nano-sized grains and the thickest no observable tertiary γ′ layer, segregation of Ti to nano-sized grain boundaries were observed.
5. In terms of the microstructure observations, grain refinement induced by machining was achieved by dislocation rather than twinning.

Acknowledgements

The authors acknowledge the financial support provided by the Engineering and Physical Sciences Research Council (EPSRC) and Rolls-Royce and Rolls-Royce plc. for the provision of samples. We thank Prof. Ian Jones for useful discussions.

Data availability

The data that support the findings of this study is available from the corresponding authors on request.

References

1. E.O. Ezugwu, Int. J. Mach. Tools Manuf., 45 (2005), 1353.
2. E.O. Ezugwu, Z.M. Wang, and A.R. Machado, J. Mater. Process. Technol., 86 (1999).
3. I.A. Choudhury and M.A. Baradie, J. Mater. Process. Technol., 77 (1998), 278.
4. J.K. Wong, D.A. Axinte, and P.J. Withers, J of Mater. Proc. Tech., 209 (2009), 3968.
5. C.R.J. Herbert, J.K. Wong, M.C. Kong, D.A. Axinte, M.C. Hardy, and P.J. Withers, J of Mater. Proc. Tech., 212 (2012), 1723.
6. D. Turan, D. Hunt, and D.M. Knowles, Mater. Sci. Tech., 23 (2007), 183.
7. D. Novovic, R.C. Dewes, D.K. Aspinwall, W. Voice, and P. Bowen, Inter. J of Machine Tools and Manufacture, 44 (2004), 125.
8. D.A. Axinte and P. Andrews, J of Eng. Manufacture, 221 (2007), 591.

9. S.B. Kim, A. Evans, J. Shackleton, G. Bruno, M. Preuss, and P.J. Withers, Met. Mater. Trans. A, 36 (2005), 3041.
10. L.L. Shaw, J.W. Tian, A.L. Ortiz, K. Dai, J.C. Villagas, P.K. Liaw, R.M. Ren, and D.L. Klarstrom, Mater. Sci. Eng. A, 527 (2010), 986.
11. B.J. Foss, S. Gray, M.C. Hardy, S. Stekovic, D.S. McPhail, and B.A. Shollock, Acta Mater., 61 (2013), 2548.
12. D.J. Child, G.D. West, and R.C. Thomson, Acta Mater., 59 (2011), 4825.
13. T. Kitagawa, A. Kubo, and K. Maekawa, Wear, 202 (1997), 142.
14. S.S. Bosheh and P.T. Mativenga, Inter. J of Mach. Tools and Manuf., 46 (2006), 225.
15. Y.K. Chou and C.J. Evans, Inter. J of Mach. Tools and Manuf., 39 (1999), 1863.
16. T. Hanlon, Y.N. Kwon, and S. Suresh, Scripta Mater., 49 (2003), 675.
17. H. Mughrabi, H.W. Hoppel, and M. Kautz, Script Mater., 51 (2004), 807.
18. J. C. Villegas, L. Shaw, K. Dai, W. Yuan, J. W. Tian, P. Liaw, and D. L. Klarstrom, Phil. Mag. Lett., 85 (2005), 427.
19. J.W. Tian, K. Dai, J.C. Willegas, L. Shaw, P.K. Liaw, D.K. Klarstrom, and A.L. Ortiz, Mater. Sci. Eng. A, 493 (2008), 176.
20. O.M.D.M. Messé, S. Stekovic, M.C. Hardy, and C.M.F. Rae, J. of Mater., **66** (2014), 2502.
21. J.C. Villegas and L.L. Shaw, Acta Mater., 57 (2009), 5782.
22. R.M. Saoubi, D. Axinte, C. Herbert, M. Hardy, and P. Salmon, CIRP Annals-Manufacturing Technology, 63 (2014), 61.
23. R.M. Saoubi, T. Larsson, J. Outeiro, Y. Guo, S. Suslov, C. Saldana, and S. Chandrasekar, CIRP Annals-Manufacturing Technology, 61 (2012), 99.
24. A.L. Ortiz, J.W. Tian, J.C. Villegas, L.L. Shaw, and P.K. Liaw, Acta Mater., 56 (2008), 413.
25. Z. Chen, R.L. Peng, P. Avdovic, J.M. Zhou, J. Moverare, F. Karlsson, and S. Johansson, MATEC Web of Conferences 14 (2014), 08002.
26. H. Ni and A.T. Alpas, Mater. Sci. Eng. A, 361 (2003), 338.
27. M. Sato, N. Tsuji, Y. Minamino, and Y. Koizumi, Sci. Tech. of Advan. Mater., 5 (2004), 145.
28. Z.R. Liao, M. Polyakov, R.G. Diaz, D. Axinte, G. Mohanty, X. Maeder, J. Michler, and M. Hardy, Acta Mater., 180 (2019), 2-14.
29. Z. Chen, M.H. Colliander, G. Sundell, R.L. Peng, and J.M. Zhou, Mater. Sci. & Eng. A, 684 (2017) 373-384.

30. P.W. Keefe, S.O. Mancuso, and G.E. Maurer: in Superalloy 1992, S.D. Antolovich, R.W. Stusrud, R.A. McKay, D.L. Anton, T. Khan, R.D. Kissinger, and D.L. Klarstrom, Eds., TMS, Warrendale, PA, 1992, P487-496.
31. T. Matsui, H. Takizawa, H. Kikuchi, and S. Wakita: in Superalloy2000, T.M. Pollock, R.D. Kissinger, R.R. Bowman, K.A. Green, M. McLean, S. Olson, and J.J. Shirra, eds., TMS, Warrendale, PA, 2000, p127-133.
32. S. Zaefferer, Cryst. Res. Technol., 46 (2011), 607.
33. S. Birosca, R. Ding, S. Ooi, R. Buckingham, C. Coleman, and K. Dicks, Ultramicroscopy, 153 (2015), 1.
34. A.M.Wusatowsk-Sarnek, B.Dubiel, A.Czyrska-Filemonowicz, P.R.Bhowal, N.Ben Salah, and J.E.Klemberg-Sapieha, Metall. Trans. A, 42 (2011), 3813.
35. E. Korznikova, E. Schafler, G. Steiner and M. J. Zehetbauer: in 'Ultrafine grained materials IV', (ed. Y. T. Zhu et al.), 97–102; 2006, Warrendale, PA, TMS.
36. J. Du, Z.Q. Liu, and S.Y. Lv, Applied surf. Sci., 292 (2014), 197.
37. L.Z. Zhou and V. Luping, J. Mater. Sci. Technol., 17 (2001), 633.
38. F.J. Humphreys and M. Hatherly: Recrystallization and Related Annealing Phenomena, Perganmon, Elsevier Sicence Inc. Tarrytown, NY, 1996, P 271.
39. N.R. Tao, X.L.Wu, M.L.Sui, J. Lu, and K.Lu, J. Mater. Res., 19 (2004), 1623.
40. L.E. Murr, in Interfacial Phenomena in Metals and Alloys (Tech-books, Herndan, VA, 1975), P.145.
41. H.W. Zhang Z.K. Hei, G. Liu, J. Lu, and K. Lu, Acta Mater., 51 (2003), 1871.
42. L.E. Murr, Thin solid films, 4 (1969), 389.

Table 1 Chemical composition of the 720Li alloy (wt.%)

Cr	Co	Ti	Mo	Al	W	Zr	B	C	Ni
16	15	5	3	2.5	1.25	0.035	0.015	0.015	Bal.

Table 2 Average grain and precipitate sizes in 720Li alloy

Matrix-γ	Primary-γ′	Secondary-γ′	Tertiary-γ′
12 ± 4.0 μm	3.7 ± 1.0 μm	440 ± 100 nm	71.5 ± 10 nm

Table 3 Average grain size (nm) estimated from the TEM of the machined surface

Slightly damage specimen	Damage specimen	
	Normal region	Ramp
21 ± 5	41 ± 19	180 ± 56

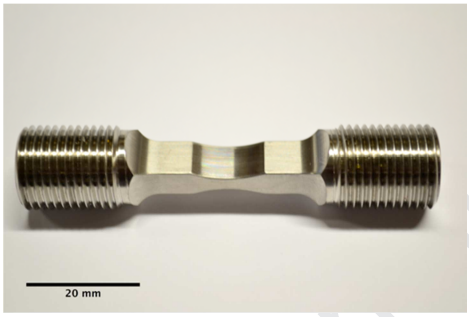

(a)

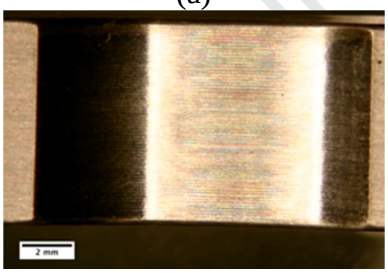

(b)

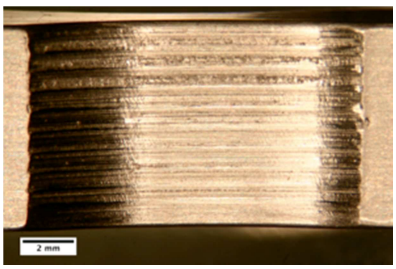

(c)

Figure 1 (a) Kt 1.1 test piece, optical images of (b) slightly damaged and (c) damaged machined sample.

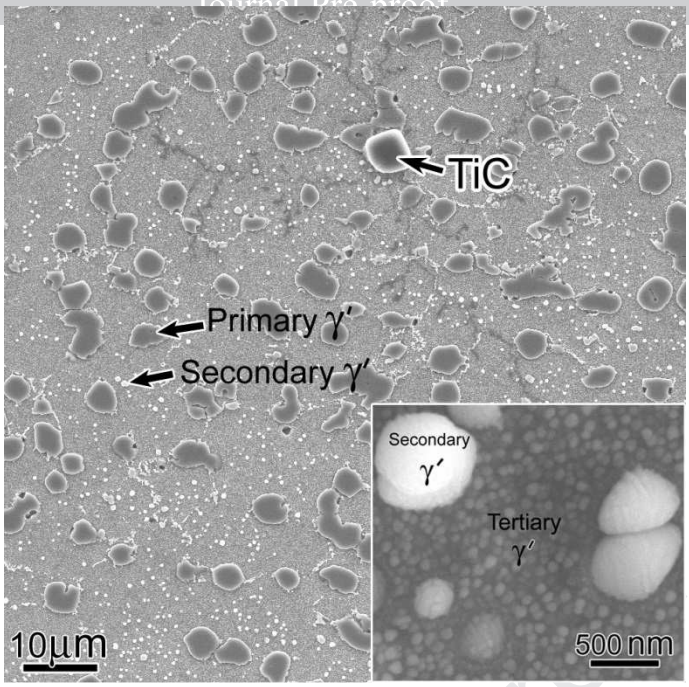

Figure 2 SEM image showing the morphology of the primary and secondary γ′ precipitates and large TiC precipitates. Inset is high magnification image showing the morphologies of secondary and tertiary γ′ precipitates.

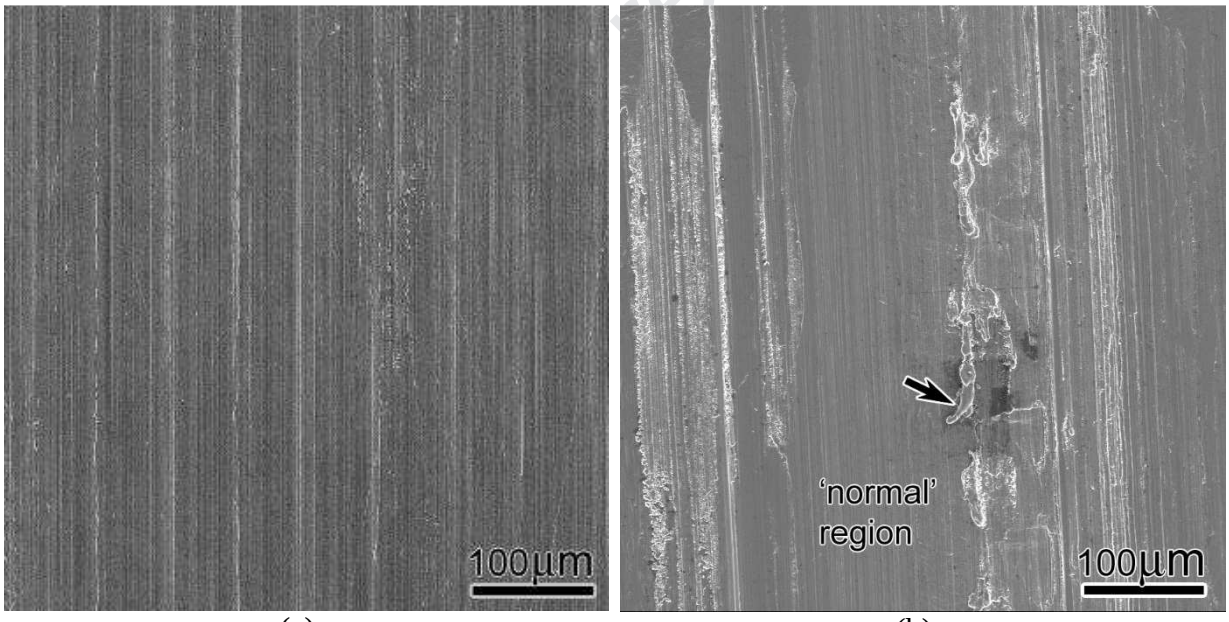

(a) (b)

Figure 3 SEM images taken from the surfaces of the (a) slightly damaged and (b) damaged specimens, showing machining marks and defects (arrowed in fig. 3b).

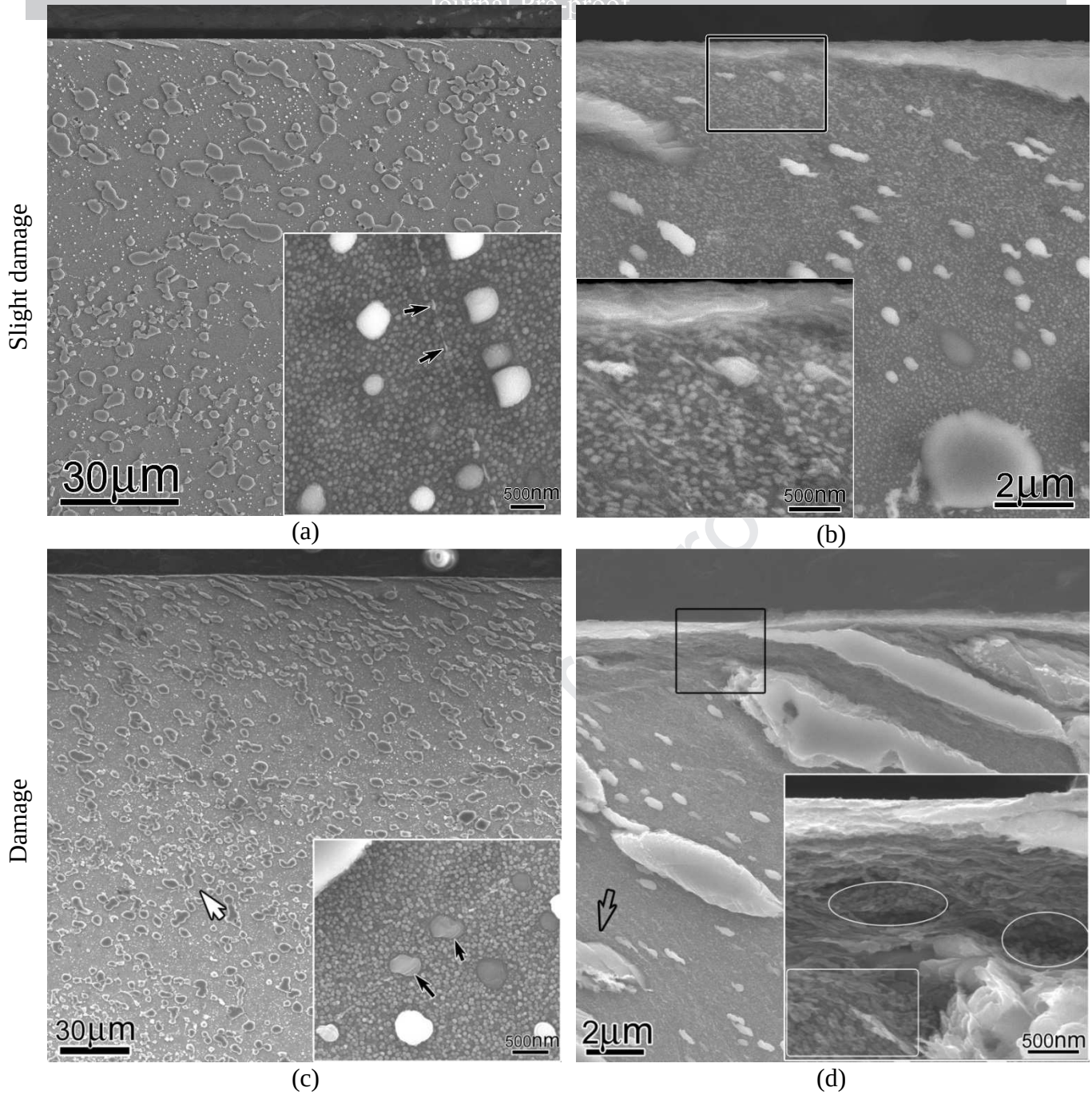

Figure 4 SEM images taken from the slightly damaged (a and b) and damaged (c and d) specimens. Inset to fig. 4a taken 33 μm away from the surface, showing a shear band (arrowed). Inset to fig. 4b taken from the marked area in no observable Fig. 4b, showing severely deformed secondary and tertiary γ′ precipitates and a ~ 400 nm wide layer (from the surface) with no observable γ′ precipitates. Inset to fig. 4c taken from the region arrowed in white (140 μm away from the surface), showing sheared secondary and tertiary γ′ precipitates. The arrow in fig. 4d indicates severely sheared γ′ precipitates; the wavelike bands observed in the inset to fig. 4d was taken from the marked rectangle in fig. 4d; the areas circled in white in the inset to fig. 4d show visible tertiary γ′ precipitates.

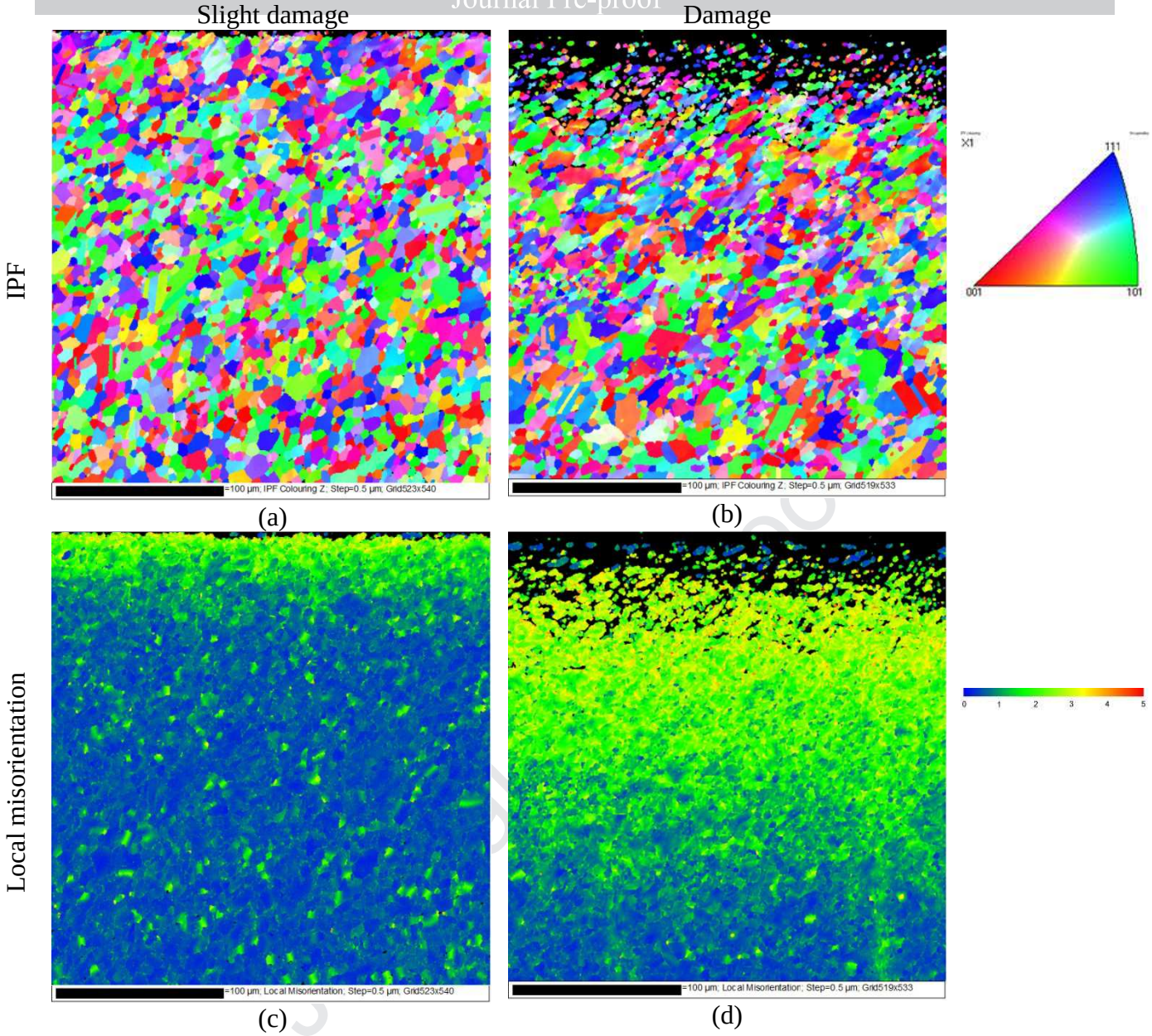

Figure 5 EBSD inverse pole figure (IPF) and local misorientation maps of deformed areas near the machined surface, (a, c) slight damage specimen and (b, d) damage specimen.

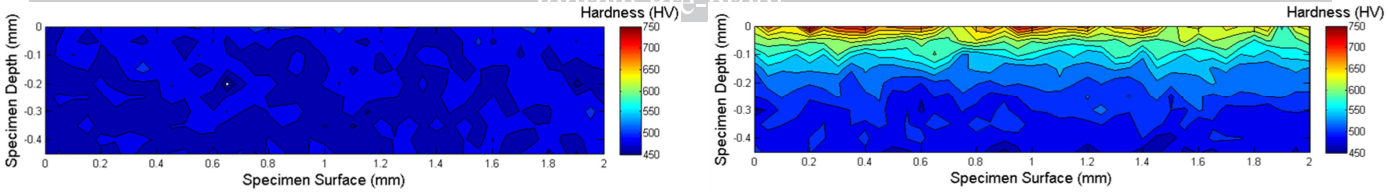

(a) (b)

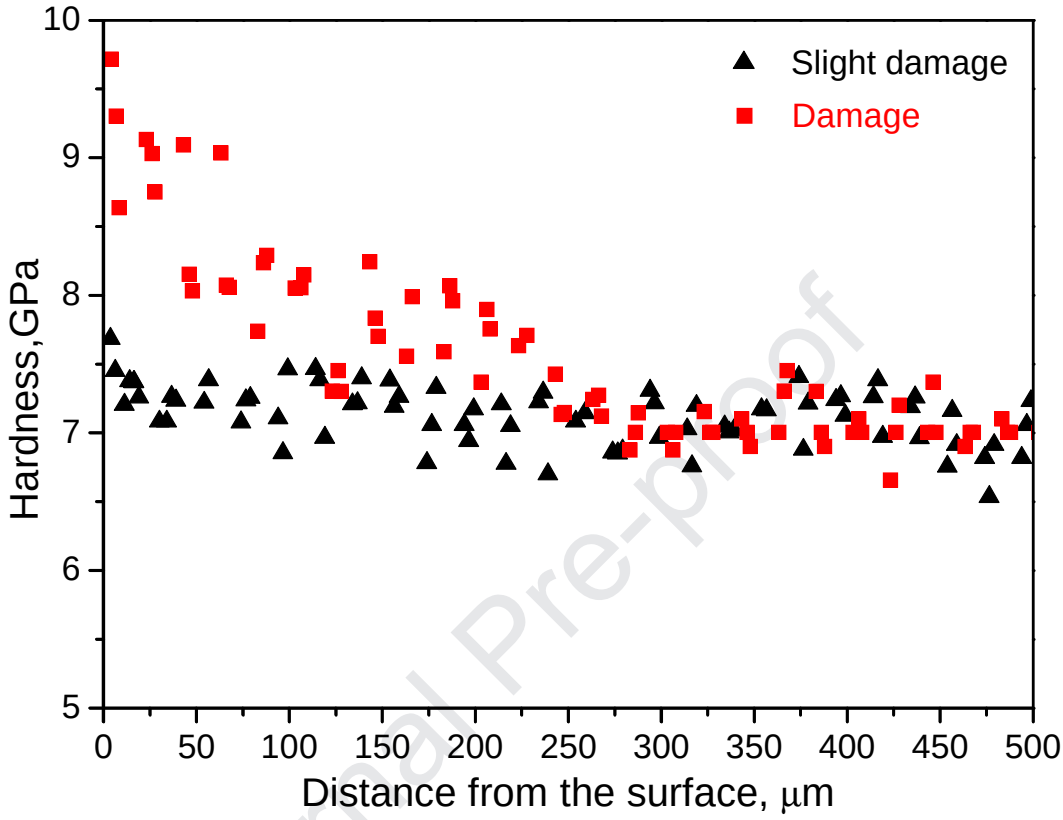

(c)

Figure 6 Micro-indenter hardness maps for (a) slightly damaged and (b) damaged samples, and (c) nano-indenter hardness profiles.

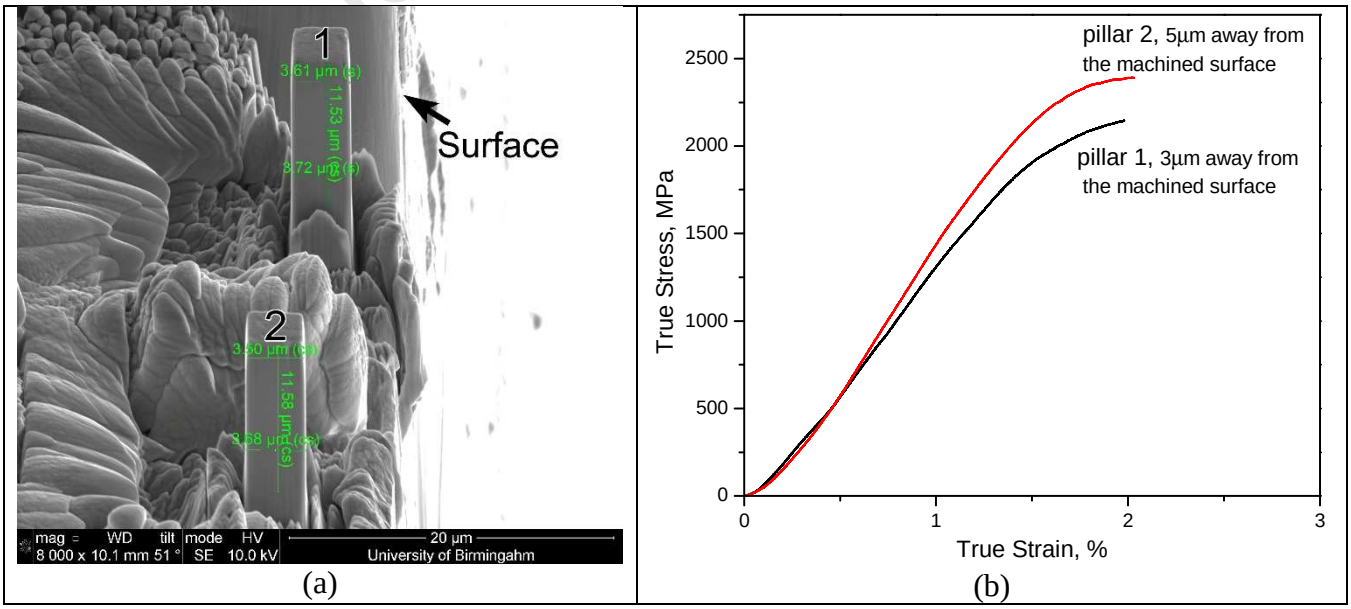

(a) (b)

Figure 7 SEM images of the square pillars machined from the severe deformation layer of the damage sample (a) and true stress-strain curves of the pillars (b)

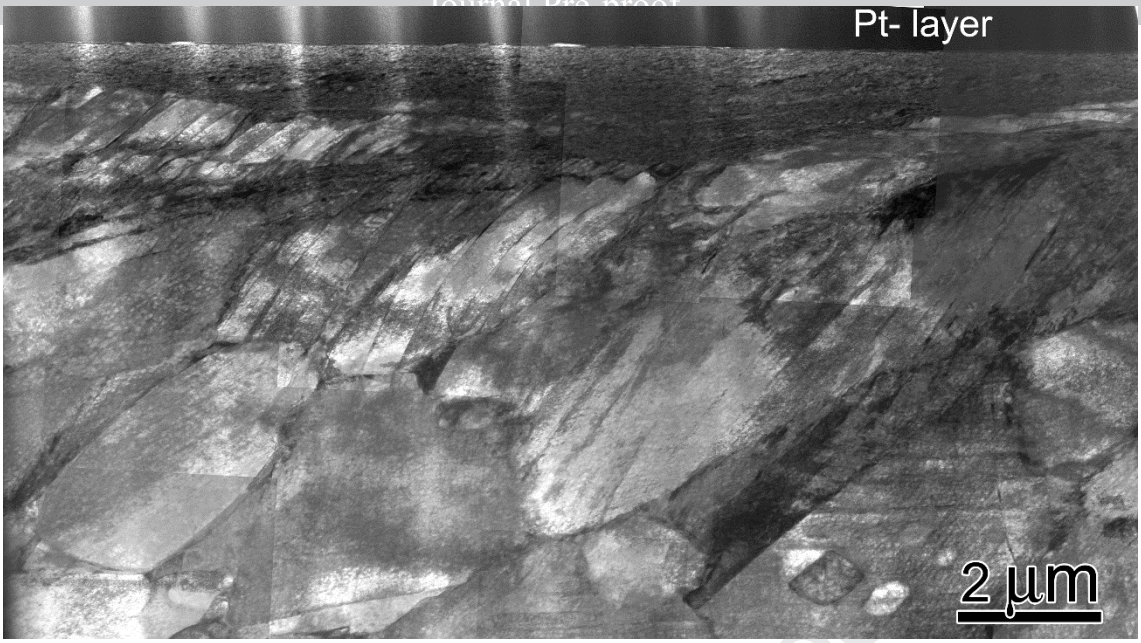

(a)

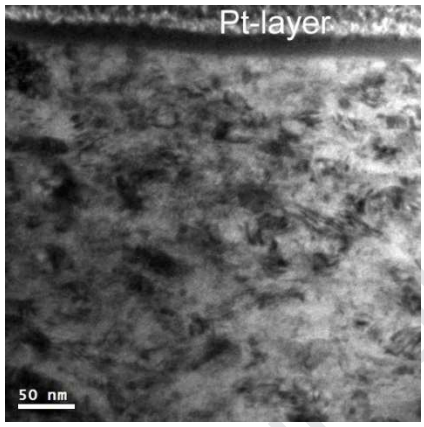

(b)

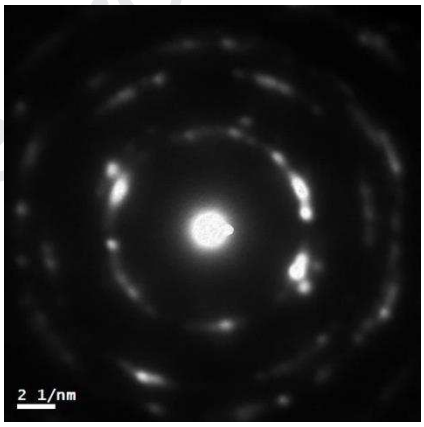

(c)

Figure 8 (a) A montage of BF-STEM images taken from the slight damage specimen, (b) A TEM image taken from the top surface of fig. 8a, and (c) an SAD pattern taken from fig. 8b.

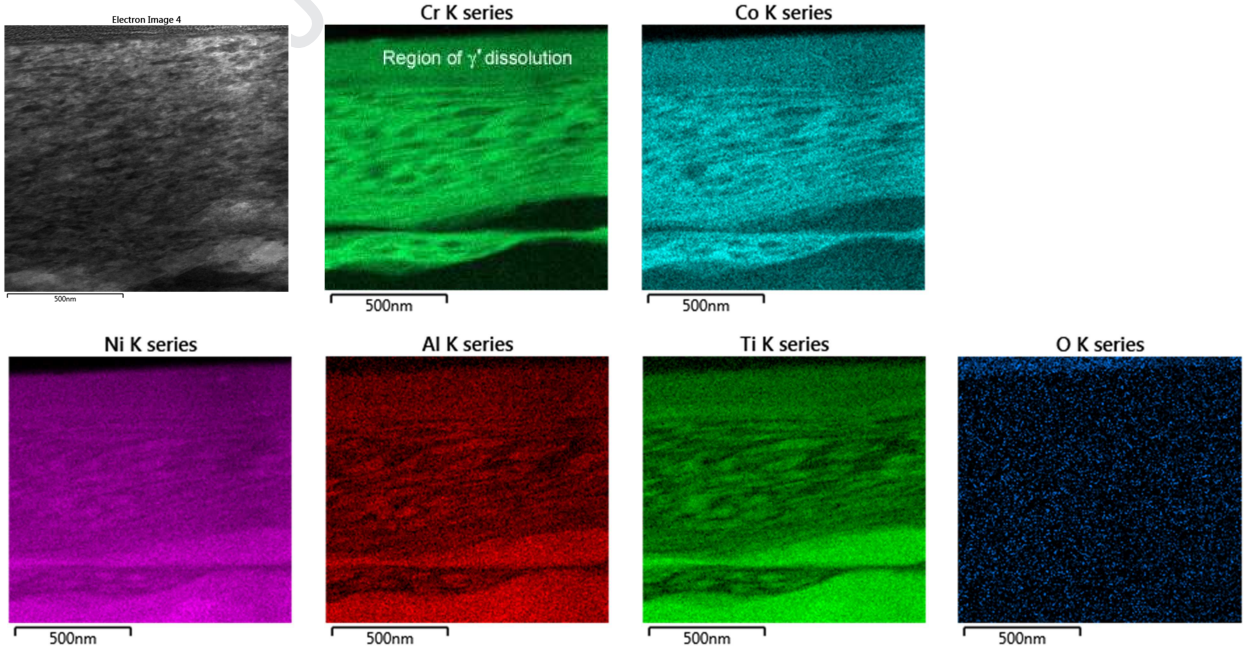

Figure 9 EDS maps from top surface of fig. 8a. Note: the γ phase is rich in Cr and Co while the γ′ phase is rich in Ni, Al and Ti.

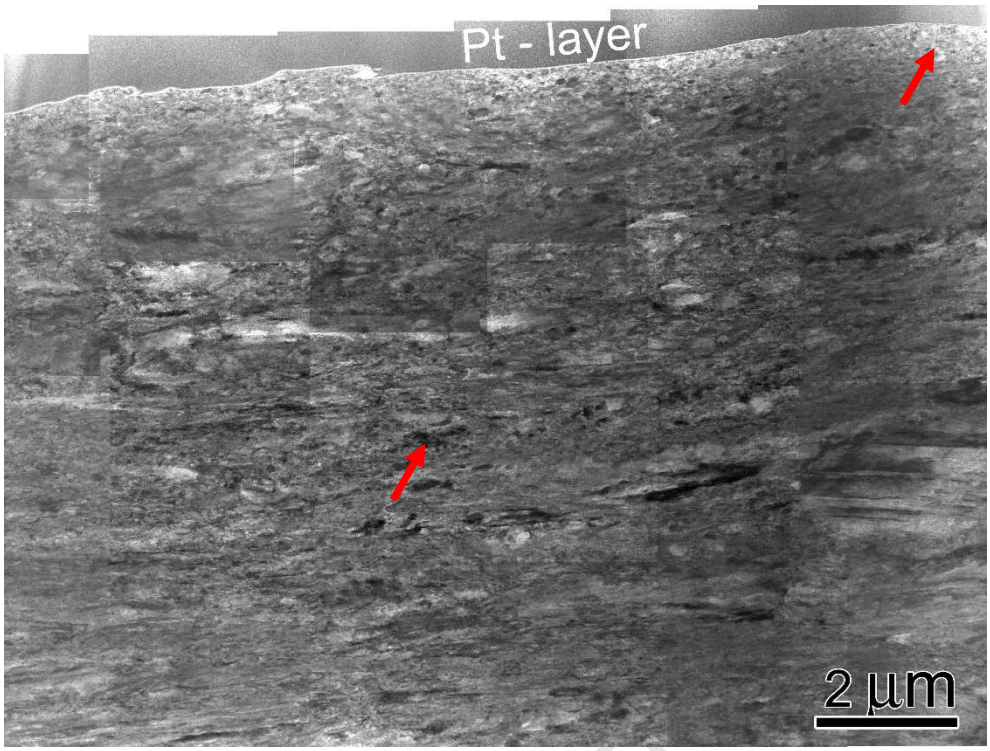

(a)

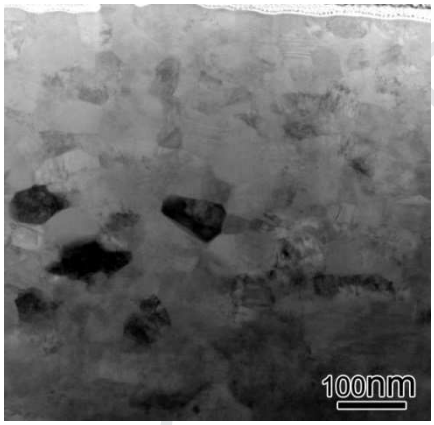

(b)

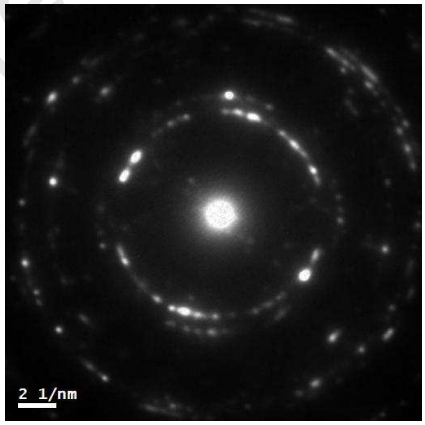

(c)

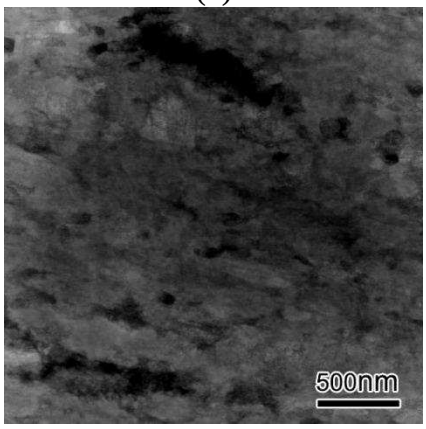

(d)

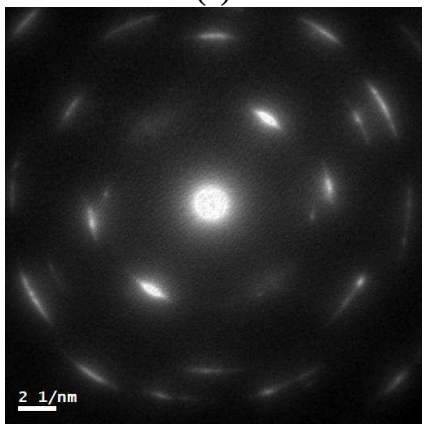

(e)

Figure 10 (a) A montage of BF-STEM images taken from the 'normal' region of the damaged specimen, (b) A TEM image taken from the top position (arrowed) of fig. 10a, (c) SAD pattern from fig. 10b, (d) A TEM image taken from the middle position (arrowed) of fig. 10a, and (e) SAD pattern from fig. 10d.

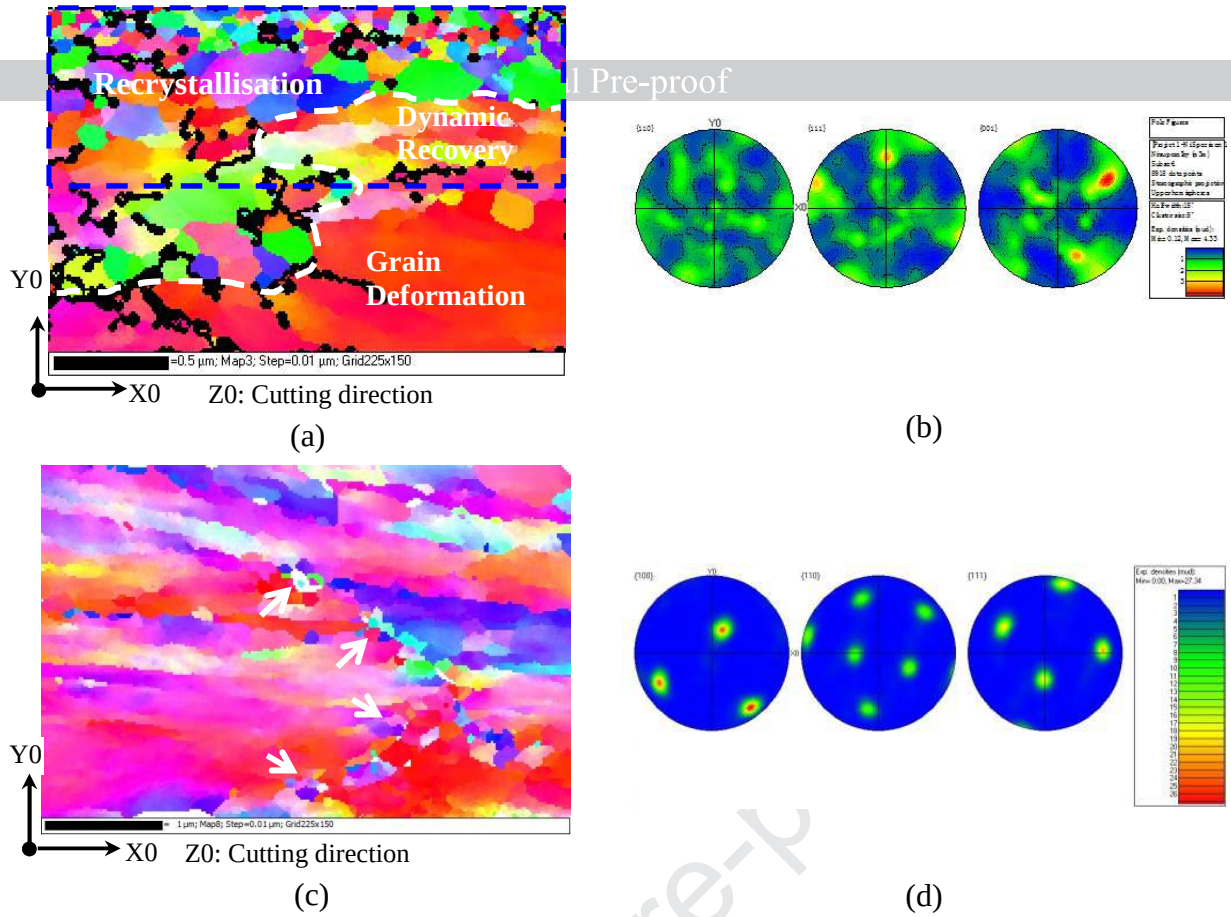

Figure 11 (a) Inverse pole figure map from the top of fig. 10a, clearly showing three regions: recrystallisation, dynamic recovery and grain deformation, (b) pole figure of the rectangular region marked in fig. 11a showing a weak texture (~ 4 times random), (c) inverse pole figure map from the middle of fig. 10a, and (d) pole figure of fig. 11c, demonstrating that most grains in fig. 11c are subgrains. Note: The region marked via white dash lines in fig. 11a is a recrystallisation region. The black regions in fig. 11a are non-indexable. The formation of fine grains probably occurs on a prior austenite grain boundary (arrowed in fig. 11c).

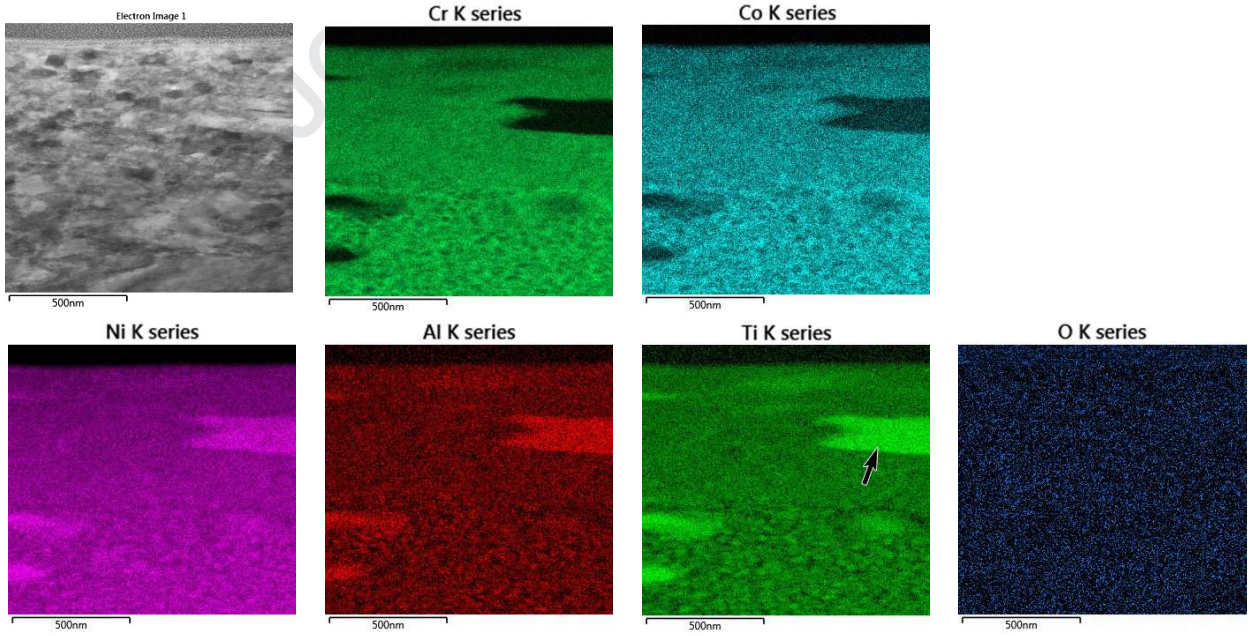

Figure 12 EDS maps from the top surface of the 'normal' region of the damaged specimen, showing a ~ 600 nm thick area without the original tertiary γ′ particles but with elongated secondary (arrowed) γ′ particle. In the region below that, the size of the small γ′ particles is ~ 30 nm, which is much smaller than the size of the original tertiary γ′ particles (71.5 nm) shown in fig. 2.

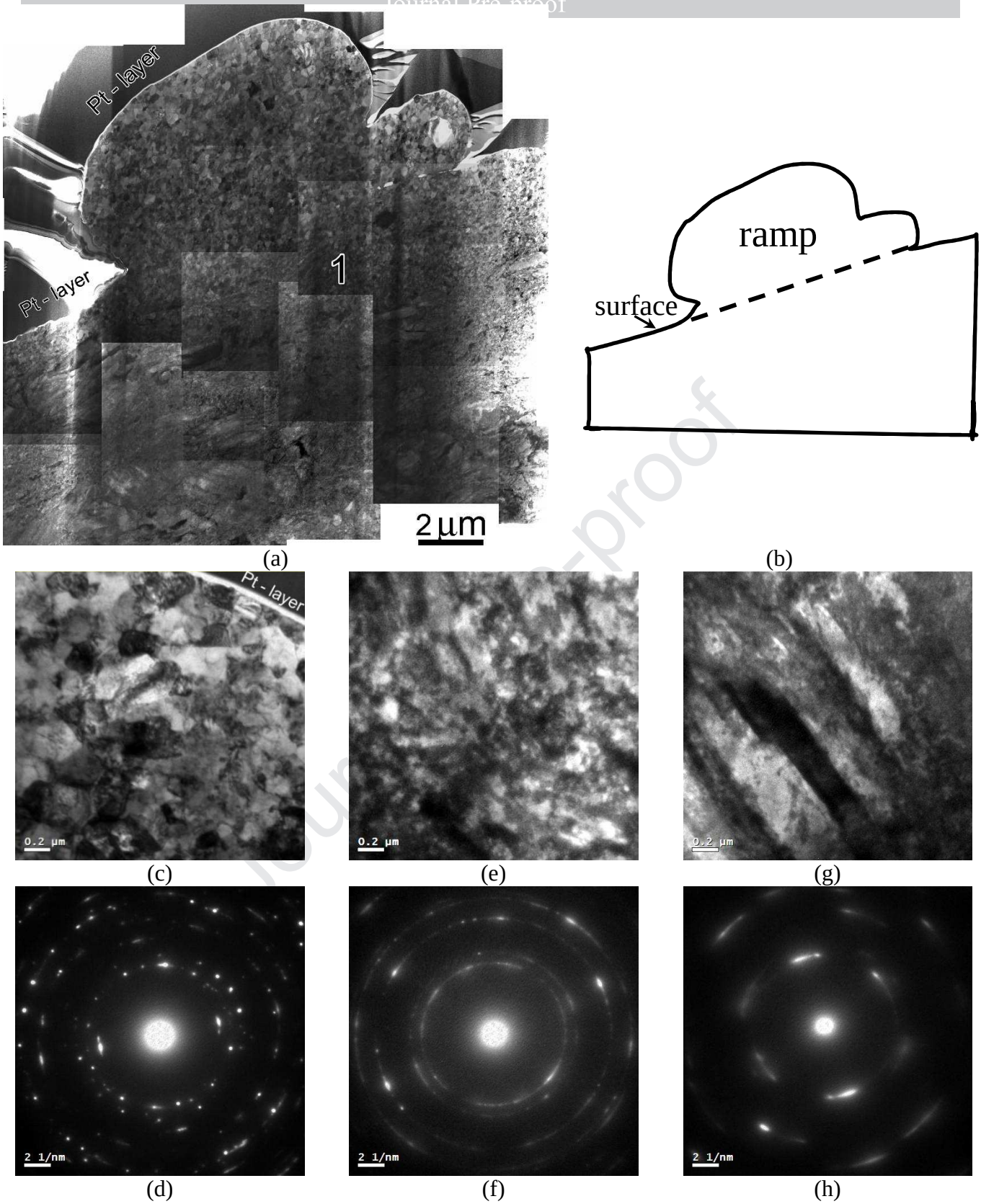

Figure 13 (a) A montage of BF-STEM images taken from a ramp of the damaged specimen, (b) a schematic of the ramp, (c) a TEM image taken from the surface of the ramp, (d) an SAD pattern from fig. 13c, (e) a TEM image taken from the middle of fig. 13a, (f) the SAD pattern from fig. 13e, (g) a TEM image taken 14 µm away from the surface of the ramp, and (h) the SAD pattern from fig. 13g.

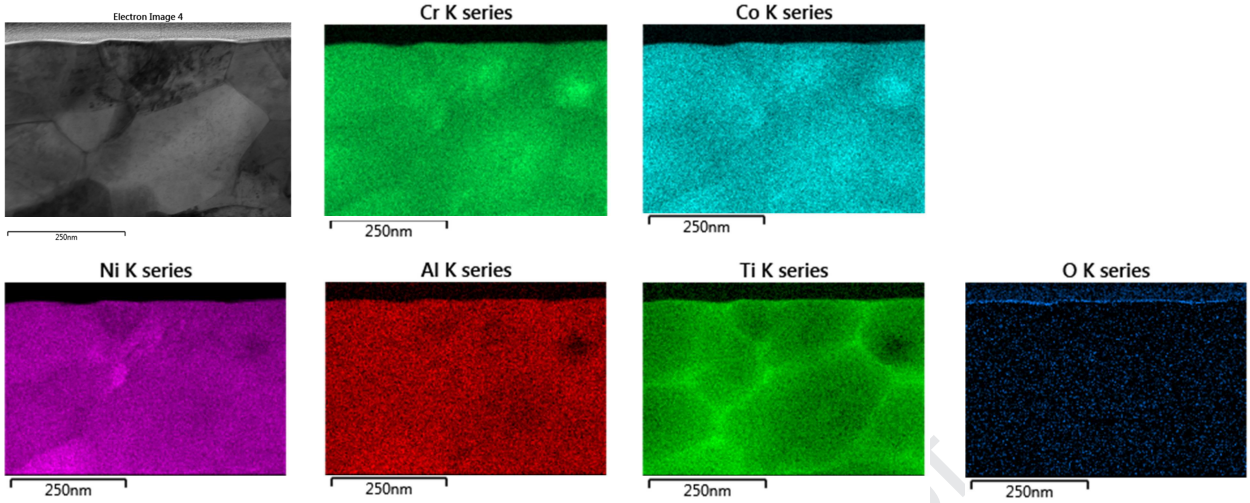

Figure 14 EDS maps for the surface of the ramp in the damage specimen, showing Ti enrichment at grain boundaries.

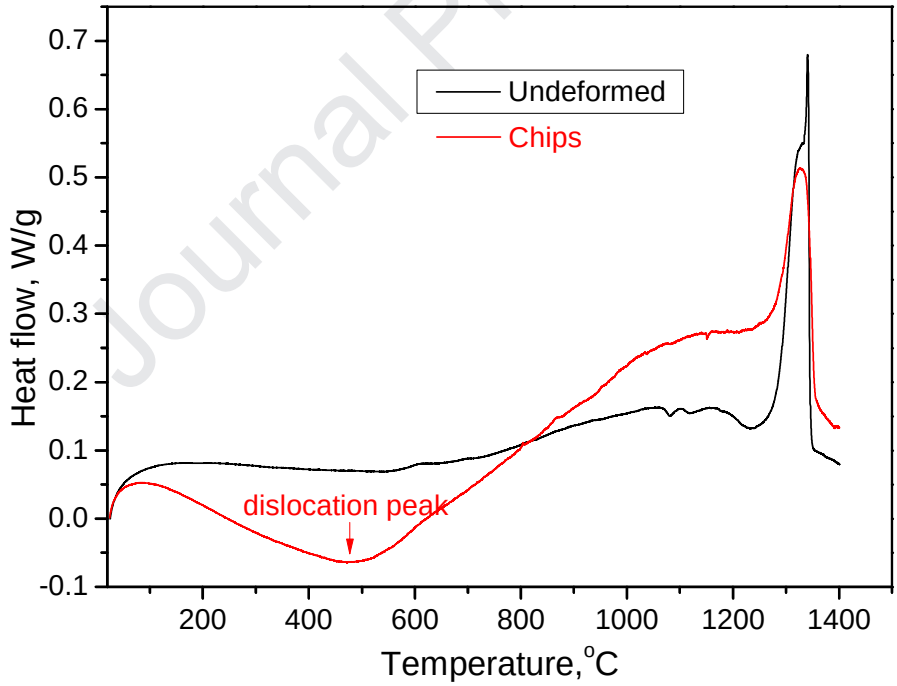

Figure 15 Differential scanning calorimetry curves with a heating rate of 10°C/min for chips and undeformed material.

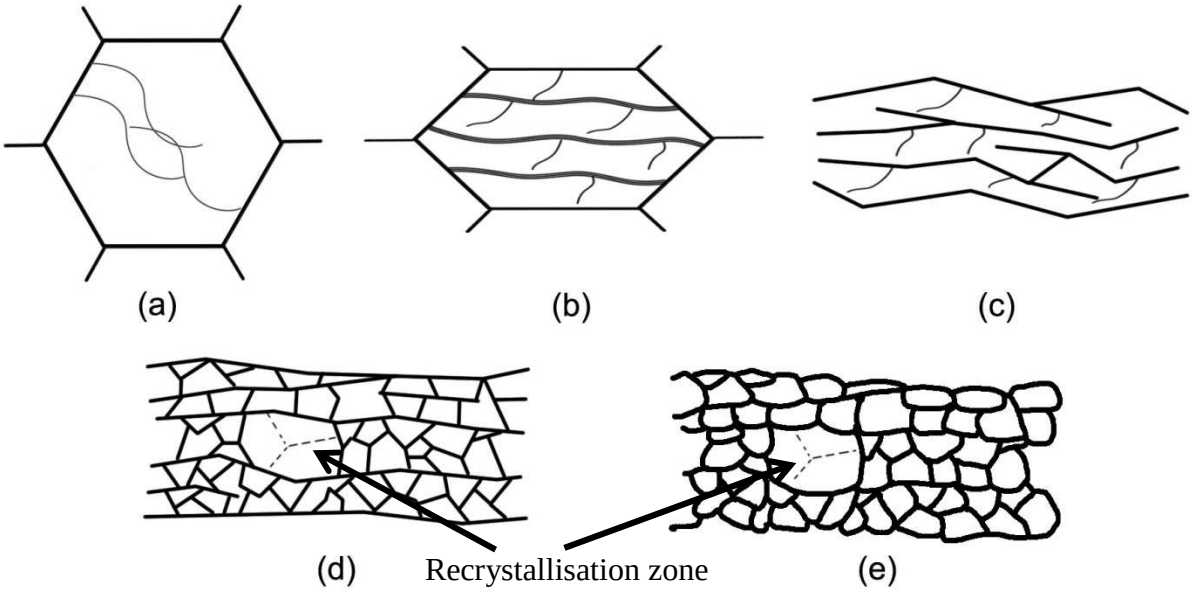

Figure 16 Schematic illustration of microstructural evolution and grain refinement induced by machining. (a) original equiaxed and coarse-grained microstructure with some dislocations, (b) original grains elongated along the shear plane and elongated dislocation cells formed within grains via generation of new dislocations, (c) well developed elongated dislocation cells with dense dislocation walls, (d) nano-sized grains with sharp boundaries formed via reorganising the dislocations within the elongated tangled dislocation cells; some grains started to recrystallise, (e) well developed nano-sized grains with occasional recrystallization and growth.

To whom it may concern

12th Nov. 2019

Dear Sir/Madam

Re: Characterization of plastic deformation induced by machining in a Ni-based superalloy

The authors declare that they have no known competing financial interests or personal relationships that could have appeared to influence the work reported in this paper

Yours sincerely,

R. Ding